Quantitative Characterization of Marble Natural Aging through Pore Structure Image Analysis

MT15161

Quantitative Characterization of Marble Natural Ageing through Pore Structure Image Analysis

Costanzo Peter[1], Eloisa Salina Borello[2], Oliviero Baietto[3], Rossana Bellopede[4], Filippo Panini[5], Alice Massimiani[6], Paola Marini[7], Dario Viberti[8]

1 Center for Sustainable Future Technologies, Fondazione Istituto Italiano di Tecnologia, Via Livorno 60, 10144, Turin, Italy

(corresponding author): costanzo.peter@iit.it

2 Politecnico di Torino, C.so Duca degli Abruzzi, 24, 10129, Turin, Italy

eloisa.salinaborello@polito.it

3 Politecnico di Torino, C.so Duca degli Abruzzi, 24, 10129, Turin, Italy

oliviero.baietto@polito.it

4 Politecnico di Torino, C.so Duca degli Abruzzi, 24, 10129, Turin, Italy

rossana.bellopede@polito.it

5 Politecnico di Torino, C.so Duca degli Abruzzi, 24, 10129, Turin, Italy

filippo.panini@polito.it

6 Politecnico di Torino, C.so Duca degli Abruzzi, 24, 10129, Turin, Italy

Alice.massimiani@polito.it

7 Politecnico di Torino, C.so Duca degli Abruzzi, 24, 10129, Turin, Italy

paola.marini@polito.it

8 Politecnico di Torino, C.so Duca degli Abruzzi, 24, 10129, Turin, Italy

dario.viberti@polito.it

Abstract

The goal of this study is the quantitative characterization of the degree of natural alteration of marble samples by using image analysis for the automatic characterization and comparison of the pore structure of rock samples before and after weathering. The proposed methodology is based on a pore exploration path finding algorithm for the identification of paths developing within the porous domain of marble samples in both natural conditions and after weathering. Along each identified path the pore radius is measured providing a thorough description of the pore space statistical distribution. The A* path finding approach was developed and applied to binarized images obtained from 2D thin sections of marble samples in both natural conditions and after 10 years of natural decay. The results are expressed in terms of 2D porosity and statistical distributions of the pore radius of the samples pre and post weathering. A comparison with the information obtained from standardized laboratory tests used for the physical and mechanical characterization of stone material is also provided. From a computational point of view, the presented approach is highly parallelizable. The presented approach works wells in complex porous structures characterized by high path tortuosity, pore size heterogeneity and pore surface roughness. Moreover, the methodology is less affected by small-scale pore features and noise, produced during image binarization, compared to other algorithms for pore structure morphological analysis such as skeleton-based and maximal ball approaches.

Keywords: marble weathering, pore network characterization, path finding, pore radius, image analysis

1 Introduction

The degradation of natural stone materials due to the interaction with the surrounding environment is strongly affected by the chemical and mineralogical composition and the physical-structural properties of the material. The active degradation processes are mainly governed by the microclimatic conditions of the environment (i.e., temperature, humidity, wind, rainfall), the conditions of installation and surface smoothing. One of the agents responsible for the degradation of stone materials is water, which can act, either directly or indirectly, through rainfall, condensation, humidity and/or rising humidity. Those alterations occur over a long period of time and mainly affect the external surface of the stone (Franzen and Mirwald, 2004).

The quantity and structure of the voids inside the stone change with decay (Nicholson, 2001) and the measurement of porosity provides the degree of this transformation (Da Fonseca et al., 2021; Çelik and Sert, 2021). The deterioration of the stone slabs, used in construction as external cladding, affects stone mechanical resistance

because the increase in porosity deriving from decohesion produces a decrease in mechanical resistance (Ju et al., 2022; Ferrero et al., 2014). The relation between stone porosity and decay has been investigated by studying the petrographic features and bowing phenomenon for over 30 years (Winkler, 1985; Grelk et al., 2007; Schouenborg et al., 2007; Marini and Bellopede, 2009; Sousa et al., 2021). Physical and mechanical stone characterization is conventionally carried out through standardized laboratory tests. Porosity can be evaluated through the measurement of Open Porosity (EN 11936), expressing the volume of the open pores present on the surfaces of the specimen, and Water Absorption (EN 13755) indicating the mass of water that can enter through the open pores (Winkler, 1985; Ozcelik and Ozguven, 2014; Aral et al., 2021). Other tests for porosity estimation are Hg intrusion porosimetry (also named MIP), polarized light and fluorescent optical microscopy and micro computed tomography (micro-CT) (Cnudde et al., 2009; Du Plessis. 2016; Murru et al., 2018; Scrivano et al., 2018).

The comparison of data obtained by means of the previously mentioned tests on specimens in natural and weathered conditions provides reliable indications on the physical and mechanical behavior of rock allowing to foresee the weathering resistance of the analyzed stone. However, Cnudde et al. (2009) found that the direct correlation between micro-CT and MIP data with total porosity and pore-size distribution curves, is difficult.

Automated approaches for quantifying stone weathering from porosity through image analysis have been proposed (Buckman et al., 2017; Datta et al., 2016; Pal et al., 2022 and reference therein). However, for a more through description of stone alteration, porosity should be coupled with a more local evaluation of the change in the pre- and post-weathered pore size pore distribution.

Several geometric methods based on pore structure extraction from 2D and 3D image analysis are proposed in the literature. Among others, segmentation-based algorithms (Øren and Bakke, 2003; Sheppard et al., 2004; Rabbani et al., 2014; Gotstick, 2017; Xu et al., 2020) allow the determination of the pore connectivity and calculation of the pore radius on segmented pore portions. However, these algorithms are sensitive to pore surface roughness and need supervision during image binarization (Wang et al., 2020). The fractal geometry approach (Xu and Yu., 2008; Xiao et al., 2019; Cai et al., 2019), and percolation theory (Liu et al., 2014 and references therein) are mainly used for total porosity and permeability estimation. Algorithms for pore skeleton extraction such as medial-axis (Lindquist et al., 1996), medial surface (Al-Raoush and Madhoun, 2017), and thinning process can be coupled with post-processing routines for pore radius estimation (Liang et al., 2019). However, these approaches can underestimate the size of the pores especially when a second medial axis junction is present within the node radius (Wang et al., 2020). Moreover, they are very sensitive to minor object boundary perturbations caused by image discretization, binarization and noise (Shaked and Bruckstein, 1998). Pore structure can be characterized through the Maximal Ball Method which consists in clustering balls into pore throats according to their sizes (Arand and

Hesser, 2017). However, this method can underestimate the pore space when it is tortuous (Wang et al., 2020). Convolutional neural networks (CNN) can be used to estimate porosity, average pore size and specific surface of the porous rocks (Alqahtani et al., 2020) as well as to estimate morphological, hydraulic, electrical, and mechanical characteristics based on micro-tomography images of porous geo-materials (Rabbani et al. 2020). The CNN approach is extremely fast but it needs to be trained on a large dataset of images. The availability of the images of stone before and after natural weathering is very limited; the application of data augmentation techniques is not recommended because of the lack in diversity of the available images (Shorten et al. 2019).

A promising approach is based on the A*path finding method to explore the porous domain using binarized images. The A* algorithm allows the identification of paths developing within the porous domain in which fluid circulation can occur. The identified paths can be exploited to estimate various geometrical parameters characterizing the porous space such as tortuosity, effective porosity and permeability from 2D and 3D binary images of well-connected rock samples (Viberti et al., 2020; Salina Borello et al., 2022).

In this study a revisited version of the approach presented by Viberti et al. (2020) is adopted to quantitatively characterize the pore structure of 2D images of marble samples before and after 10 years of natural decay. The advantage of using the A* is that the algorithm is less affected by complex pore structure, having high path tortuosity, pore size heterogeneities and pore surface roughness, compared to skeleton-based and maximal ball approaches. Results are compared with degradation information obtained by standard experimental procedures (variations in ultrasound propagation speed, variation in flexural strength, and water absorption) in order to verify if the variations of the physical parameters obtained with standard laboratory tests are in agreement with the variations of the parameters evaluated with the use of the * A algorithm.

2 Materials and Methods

2.1 Rock sample description

The analyzed rock, named C1, is a white marble with light gray veins (Fig.1) obtained from the Tuscan extracting basin. The composition of the marble is predominantly calcitic with some dolomitic rhombic crystals. Quartz is instead present as an accessory mineral. The marble is made up of subhedral blasts sometimes interlobated with dimensions ranging from 300 to 600 microns approximately with a slightly anisotropic microstructure.

One sample of the marble studied in this work (C1) was exposed to external degradation agents for about ten years on the roof of the DIATI (Environmental, Land and Infrastructure Engineering Department) at the Politecnico di Torino, while the other sample comes from a slab of the same marble in natural condition.

2.2 Physical and mechanical tests

The physical and mechanical stone characterization is carried out through conventional and destructive tests such as flexural strength coupled with non-destructive tests such as ultrasonic pulse velocity and water absorption performed in the laboratory by means of standardized tests (EN 14579, UNI EN 12372, UNI 11432, EN 13755). Two water absorption tests were carried out: water absorption (WA) by means of a contact sponge and water absorption (Ab) at atmospheric pressure. They are simple and cheap standardized approaches used for testing natural stones, widely used in stone laboratories as it is required for the CE marking.

All tests were performed both on weathered and non-weathered samples of C1 with dimensions according to standars of each test described in the following sections

2.2.1 Variations in ultrasound propagation speed – UPV

The UPV (Ultrasonic Pulse Velocity) test is a fast and efficient non-invasive approach for defining the mechanical properties of a stone material. This method is based on the principle of the propagation of mechanical oscillations in the ultrasound field: a transducer held in contact with the surface of the test material produces ultrasounds, which after having crossed a path of known length within this material, are received from a second transducer and converted into an electrical signal. It is possible to determine the characteristic speed of the material once the time needed to cross this space is calculated. This speed is linked to the type of material and to its physical and mechanical characteristics such as the crystalline structure, porosity and cohesion (Rasolofosaon et al., 2000). The alteration of the properties of the material which underwent natural deterioration can be analyzed by comparing the propagation speed of the weathered sample with the original one characterized by unaltered properties. The degradation progress of the material is associated to a worsening of its mechanical characteristics and, consequently, to a lowering of the ultrasound propagation speed compared to the one measured in the unaltered sample. The test has been carried out on 10 specimens. The test results indicate that the measured propagation of ultrasounds obtained from indirect method (EN 14579 (2005) standard) shows consistent variations in speed between altered and unaltered specimens (Tab. 1).

2.2.2 Variation in flexural strength

Flexural strength is defined as the resistance of a material to the forces that tend to bend it. This test is based on the principle that a body undergoing a bending stress, due to the constraints to which it is subjected, reacts by

opposing a system of forces applied by means of a mechanical press, which would tend to make it rotate around one of its points. The methods of carrying out the flexural strength test are described by the European Standard UNI EN 12372 (2001). The test has been carried out on 10 specimens. Results are reported in Tab. 2.

2.2.3 Variation of water absorption (WA) by means of a contact sponge

Water absorption by contact sponge is a quick test which can be carried out directly in situ and is part of the Italian Cultural Heritage standards. The contact sponge method is used to determine the amount of water absorbed by the stone material per surface unit as a function of a pre-determined time interval equal to 60 seconds. The test is carried out, both in the laboratory and in situ, on flat surfaces and the procedure is described in the Italian standard UNI 11432 (2011). Through this test, it is possible to make qualitative considerations on the degree of absorption of the material at its surface and to compare the variations of this parameter on altered and unaltered specimens. The test has been carried out on 10 specimens. The results are reported in Tab. 3.

2.2.4 Variation of water absorption (Ab) at atmospheric pressure.

Water absorption capacity *Ab* is represented by the percentage ratio between the mass of water absorbed and the dry weight of the specimen. This value is determined by following the procedure described in the European Standard UNI EN 13755 (2001). The results allow a direct comparison between the characteristics of the non-degraded and degraded material, both within it and on its surface. The test has been carried out on 10 specimens. Results are reported in Tab. 4.

2.2.5 Discussion

All the physical tests carried out on the weathered and non-weathered specimens show how there is significant increase in water absorption both at atmospheric pressure and by means of a contact sponge in the specimen that underwent natural aging. The values of flexural strength and speed of propagation of ultrasonic waves confirm a worsening of the mechanical characteristics of the specimen subjected to aging.

2.3 Pore structure characterization from image analysis

The characterization of the rock pore structure is obtained by analyzing a number of binarized microscope images acquired from 2D thin sections obtained from impregnated specimens: a horizontal section on the non-weathered

specimen (initial), three horizontal sections taken at different depths (epar1, epar2 and epar3) from the weathered specimen, and a vertical section (transv) taken from the weathered specimen (see fig. 4). The impregnation process was carried out with epoxy resin and methylene blue, repeatedly, under vacuum in order to obtain a smooth surface, when viewed under the macroscope. Each image is processed for the identification and characterization of paths developing within the porous domain through a revisited version of the approach presented by Viberti et al. (2020). This technique was successfully used by the authors to estimate tortuosity, effective porosity and permeability from 2D binary images of well-connected rock samples. Here the methodology has been revisited to allow a good exploration of poorly connected samples/areas, focusing on pore size characterization.

The adopted workflow is qualitatively described in the flow chart in Fig. 2.

2.3.1 Image acquisition and binarization

Thin sections of marble samples described in paragraph 2.1, representative of pre- and post-weathering conditions, were analyzed and compared. The images were acquired using a Leica MZ6 macroscope (40X magnification) and photographed by means of the Panasonic Lumix CMD-GF6 digital camera in *.tiff format at 12 Mpixels, with an image resolution of 0.8 μm per pixel. Square subsections of 2.47 mm per side were extracted to avoid the peripheral darkening (vignetting) reproducing the optical edge of the macroscope's light path. Digital processing was then applied to the images to highlight and extrapolate the impregnated paths according to the following steps:

1. Preliminary tuning of image parameters such as intensity, gamma, saturation, brightness and contrast is applied to highlight the impregnated paths: originally blue on a gray background, impregnated paths become light green on a purple background (see Fig. 5).
2. Gauss blur (μ=0, σ=3) is applied to avoid artificial path fragmentation due to noise.
3. Image is binarized according to a color-based mask:
    a. Being the impregnated paths green, a greenness index (i_g) is calculated for each pixel:

$$i_g = \frac{g}{r+b} \quad (1)$$

    Where r, g and b are the normalized RGB components of the images. The color index approach is borrowed by image analysis of microfluidics (Mauk et al., 2013).
    b. A greenness threshold (t) is fixed as the 80th percentiles of the greenness distribution within the image.
    c. All pixels with $i_g > t$ are assumed to be impregnated pixels and are assigned digital value 1

(depicted in white); all remaining pixels are assigned digital value 0 (depicted in black).

4 Bicubic interpolation with threshold 0.5 is applied to remove possible isolated pixels and to reduce the computational cost of the subsequent analysis; the final resolution of the binarized images is 4 μm per pixel.

Accuracy of image binarization was qualitatively evaluated by visual inspection. An example is shown in Fig. 6. Further insights on image binarization are beyond the scope of this work.

A number of images representing well-spaced subsections were acquired from each thin section to guarantee a statistical representativeness of the results. The number of images depends on the degree of heterogeneity of the pore network observed within the thin section e.g., higher heterogeneity requires a higher number of images to statistically represent the geometrical layout of the pore network.

High heterogeneity was observed, especially in the non-weathered and in the transversal sections. Five images were acquired for the weathered horizontal sections (epar1, epar2 and epar3), while nine images were considered for the non-weathered thin section (initial) and for the vertical (transv). The latter were divided in three groups: 3 subsections near the top (transv1), 3 in the middle (transv2) and 3 near the bottom (transv3) (see Fig. 3). This subsection grouping allows the correlation between the horizontal and transversal subsections through the association of epar1-transv1, epar2-transv2 and epar3-transv3 subsections as qualitatively shown in Fig. 4. For example, some subsections are shown in Fig. 5 while the image binarization process is shown in Fig. 6 for one subsection of transv2.

2.3.2 Path identification in the porous domain

The pore network is characterized by the identification of paths based on the approach presented by Viberti et al. (2020) which relies on the A* pathfinding algorithm (Hart et al., 1968; Nilsson, 2014). A* is widely used to search for the shortest path between a starting and an end point (Russel and Norvig, 2018). Each calculated path is represented by a continuous graph developing from an initial to a final node which are connected through a set of nodes and edges. Each node is identified by its coordinates. Only the continuous paths able to connect an initial and final node are stored and used for pore network description (Viberti et al., 2020, Salina Borello et al., 2022).

However, when dealing with a marble pore structure characterized by truncated connectivity, the application of A* to the binarized image is less effective due to the significant presence of dead-end paths (i.e., paths forming at the initial node but not reaching the associated final node). Such paths would not be stored, thus blocking the exploration of the inner part of the image. Therefore, a better characterization of the pore network of the poorly

connected areas of the image is achieved by adopting some modifications in the algorithm.

First of all, dead-end paths are recorded and accounted for. This is achieved by identifying the point at which a dead end is reached during the path construction and store the path up to that point. Furthermore, each binarized 2D image is subdivided into sub-windows Fig. 7b) and inlet/outlet nodes are identified on the opposite sub-window boundaries to investigate the path construction along the main directions (x,y). This allows the construction of paths in the inner zones of the image even if connectivity is not preserved.

For the cases presented 36 sub-windows of 0.412 x 0.412 mm were adopted as a result of preliminary sensitivities. For each of the 36 sub-windows, a set of nodes corresponding to the pore channel centers is located along the four boundaries of the sub-image considering four main path development directions (N-S, S-N, E-W, W-E). The nodes along the boundaries are then set as initial or final based on the considered direction (e.g., in the N-S scenario the initial nodes are located on the top boundary while the final nodes on the bottom boundary). Along each direction A* is run for each initial/final node pair combination giving a total number of $n_{initial}$ x n_{final} output paths for each main direction. Each path is resampled so that a path node is placed at each pixel crossed by a path (Viberti et al., 2020). Eventually, the four sets of paths (N-S, S-N, E-W, W-E) are merged for each window (Fig. 7c-e). The final output that accounts for all the 36 sub-windows is shown in Fig. 7d. The construction path process described above can be highly optimized through parallelization.

2.3.3 Pore space characterization

The analysis of the weathering effect on marble slabs is carried out through the statistical characterization and comparison of the pre- and post-weathered marble samples. Total porosity is calculated for each binarized image by simply computing the ratio between void (e.g., pores) and total image area. Furthermore, the identified paths are exploited for inner pore network characterization. The local pore radius is calculated at each path node location along each path. This is achieved by identifying the local path direction (path slope) and by counting the number of pore cells (e.g., white pixels) along the axis orthogonal to the local path direction as qualitatively shown in Fig. 8. It is possible to calculate the pore radius at a specific node location by knowing the pixel dimension. A more thorough description of the pore radius calculation is provided by Viberti et al. (2020) and Salina Borello et al. (2022). Eventually, the statistical outputs are extrapolated from porosity and pore size distributions.

3 Results and discussion

For all the analyzed images, a good pore space exploration was provided both in well-connected areas (Fig. 9c and Fig. 9e) as well as in poorly connected areas (Fig. 9a-b and Fig. 9d). Results on the total porosity distribution for

the pre- (initial) and post- weathering (epar1, epar2, epar3, transv1, transv2, tramsv3) sections are compared and summarized as percentiles (P10, P25, P50, P75 and P90) in Tab. 5, and as boxplots in Fig. 11a where the box represents the P25-P75 range, the horizontal line the P10-P90 range and the vertical line the P50. Results on pore radius distribution for the pre (initial) and post weathering (epar1, epar2, epar3, transv1, transv2, transv3) sections are compared and summarized as distribution percentiles in Tab. 6, as histograms in Fig. 10 and as boxplots in Fig. 11b.

The result comparison given in Fig. 10a and 10b shows a significant pore radius increase after weathering, especially at the bottom section (epar3). The increase of the pore radius after weathering is comparable in the median value (P50) between epar3 (20%) and epar1 (13%); the difference is more evident in the P90 where epar3 shows an increase of 30% vs. 9% for epar1. However, low percentile values are almost unchanged with respect to the non-weathered sample indicating that small pores were less affected by degradation. Conversely, the distribution on the internal section (epar2) is almost unchanged.

A coherent behavior is observed on the transversal sections (Fig. 10b), where the distribution of the bottom part (transv3) is shifted to higher pore radius values while the distribution of the middle part (transv2) is concentrated on lower pore radius values. However, as the sections were taken along the vertical direction, quantitative results are not fully comparable with the initial horizontal sections. For instance, the middle part distribution of the transversal section (transv2) shows lower percentiles with respect to the initial section for both total porosity and pore radius.

The significant change in pore structure highlighted by the pore radius distribution is confirmed by a significant increase in total porosity. By comparing total porosity calculated from the horizontal section of the non-weathered marble (initial) with sections of naturally weathered specimens (epar1, epar2 and epar3) (Fig. 11a), the porosity increase, in terms of P50, is about 90% for epar3 and 54% for epar1 and even doubled if considering P25 (about 170% for epar3 and 123% for epar1). A not negligible porosity increase is observed also in epar2, but way lower than in the other two sections.

The same trend is observed at the transversal sections: bottom subsections (transv3) show a significantly higher porosity value with respect to the other subsections (transv2 and transv1).

The detected degradation is in good agreement with the decreasing of mechanical resistance observed in experimental measurements of flexural strength and Ultrasound Pulse Velocity (Tab. 1). In fact, the increase in the average size of the pores is closely correlated both to the decrease in flexural strength and to the reduction in the ultrasound propagation speed. Moreover, the experimentally measured increase of more than 200% in water adsorption (Tab. 3 and Tab. 4) is coherent with the 170% increase of P25 of total porosity observed on epar3.

The analysis carried out when applying the A* algorithm on 2D thin section images from pre- and post- weathered marble slabs, provide a quantitative characterization of the 2D pore structure alteration. Within each identified group (top, mid, bottom in fig. 4) the corresponding epar and transversal sections show a coherent behavior. It stands to reason that a 2D analysis can qualitatively mirror a similar alteration degree of the pore structure in the three-dimensional space. However, in order to quantitatively describe the 3D pore network characteristics and the propagation of the weathering effect within the porous domain of the rock sample, a more thorough analysis would require further investigation using 3D micro-CT image as an input for A*, which could then be easily applied to the 3D rock image (Salina Borello et al., 2022).

4 Conclusions

Stone degradation induces a change in the pore structure resulting in the reduction of mechanical resistance of the material. Therefore, the evaluation of a change in porosity as well as in the pore structure can provide insights on the degree of transformation of the physical characteristics of the stone.

In this study, several samples of a marble slab, both in natural conditions and after 10 years of natural weathering, have been analyzed to study the relationship between the weathering effect and porosity and pore structure variation.

An automatic approach has been used to quantitively evaluate the pore radius distribution within the porous domain. The method has been applied to 2D binarized images obtained from the digitalization of marble thin sections pre- and post- weathering. The images were analyzed using the A* path finding algorithm. This algorithm can efficiently work with complex pore structure being less affected by the geometry of the porous domain. It is possible to calculate the local pore radius extension along each identified path. The pre- and post- weathering pore radius distribution comparison allows a quantitative evaluation of the degree of variation of the pore structure.

The results highlight an increase in water absorption which occurred naturally in the specimen at 10-year exposure compared to the non-weathered sections. The increase in the average size of the pores correlates well with the results obtained from conventional laboratory tests, which highlight a decrease in flexural strength, a reduction in the ultrasound propagation speed and an increase in water absorption.

Future work should be focused on the investigation of pore space connectivity distribution within the image. The A* can be easily applied to extract this data. Connectivity could be then coupled with pore size variation to obtain further insights on the effect of weathering to the pore structure.

Data Availability Statement

Some or all data, models, or code that support the findings of this study are available from the corresponding author upon reasonable request, such as pore throat calculation script.

References

Alqahtani N., Alzubaidi F., Armstrong R. T., Swietojanski P., Mostaghimi P., 2020. Machine learning for predicting properties of porous media from 2D x-ray images. Journal of Petroleum Science and Engineering, 184, 106514. https://doi.org/10.1016/j.petrol.2019.106514.

Al-Raoush, R. I., Madhoun, I. T., 2017. TORT3D: A MATLAB code to compute geometric tortuosity from 3D images of unconsolidated porous media. Powder technology, 320, 99-107. https://doi.org/10.1016/j.petrol.2019.106514.

Aral, İ. F., Boy, R., Dinçer, A. R., 2021. Effects of freeze-thawing cycles on the physical and mechanical properties of basaltic and dolomitic rocks evaluated with a decay function model. Bulletin of Engineering Geology and the Environment, 80(4), 2955-2962. DOI:10.1007/s10064-019-01586-z.

Arand F., Hesser J., 2017. Accurate and efficient ball algorithm for pore network extraction. Computer & Geoscience, 101, 28-37. https://doi.org/10.1016/j.cageo.2017.01.004.

Buckman J.; Bankole S.A.; Zihms S.; Lewis H.; Couple G.; Corbett P.W.M., 2017. Quantifying Porosity through Automated Image Collection and Batch Image Processing: Case Study of Three Carbonates and an Aragonite Cemented Sandstone. Geosciences, 7(3), 70. https://doi.org/10.3390/geosciences7030070.

Cai J., Zhang Z., Wei W., Guo D., Li S., Zhao P., 2019. The critical factors for permeability-formation factor relation in reservoir rocks: Pore-throat ratio, tortuosity and connectivity. Energy, Elsevier, 188, 2019, ISSN 0360-5442. https://doi.org/10.1016/j.energy.2019.116051.

Çelik, M. Y., Sert, M., 2021. An assessment of capillary water absorption changes related to the different salt solutions and their concentrations ratios in the Döğer tuff (Afyonkarahisar-Turkey) used as building stone of cultural heritages. Journal of Building Engineering, 35, 102102. https://doi.org/10.1016/j.jobe.2020.102102.

Cnudde, V., Cwirzen, A., Masschaele, B., Jacobs, P. J. S., 2009. Porosity and microstructure characterization of building stones and concretes. Engineering geology, 103(3-4), 76-83. https://doi.org/10.1016/j.enggeo.2008.06.014.

Da Fonseca, B. S., Pinto, A. F., Rodrigues, A., Piçarra, S., Montemor, M. F., 2021. The role of properties on the decay susceptibility and conservation issues of soft limestones: Contribution of Ançã Stone (Portugal). Journal of Building Engineering, 44, 102997. https://doi.org/10.1016/j.jobe.2021.102997.

Datta D., Thakur N., Ghosh S., Poddar R., Sengupta S., 2016. Determination of Porosity of Rock Samples from Photomicrographs Using Image Analysis, in: IEEE 6th International Conference on Advanced Computing (IACC), 2016, pp. 320-325, doi: 10.1109/IACC.2016.67.

Du Plessis, A., Olawuyi, B. J., Boshoff, W. P., Le Roux, S. G., 2016. Simple and fast porosity analysis of concrete using X-ray computed tomography. Materials and structures, 49(1), 553-562. https://doi.org/10.1617/s11527-014-0519-9.

EN 12372 Natural Stone Test Methods - Determination of Flexural Strength under Concentrated Load CEN Committee, Brussels, 2007.

EN 13755 Natural Stone Test Methods - Determination of Water Absorption at Atmospheric Pressure CEN Committee, Brussels, 2008, p. 8

EN 14579 Natural Stone Test Methods - Determination of Sound Speed Propagation CEN Committee, Brussels, 2005, p. 12

EN 16306 Natural stone test methods - Determination of resistance of marble to thermal and moisture cycles CEN Committee, Brussels, 2013

EN 1936 Natural stone test methods. Determination of real density and apparent density, and of total and open porosity, 2006.

Ferrero, A. M., Migliazza, M., Spagnoli, A., Zucali, M., 2014. Micromechanics of intergranular cracking due to anisotropic thermal expansion in calcite marbles. Engineering Fracture Mechanics, 130, 42-52. https://doi.org/10.1016/j.engfracmech.2014.01.004.

Franzen C., Mirwald P. W., 2004. Moisture content of natural stone: static and dynamic equilibrium with atmospheric humidity, Springer-Verlag, 46, 391-401. https://doi.org/10.1007/s00254-004-1040-1.

Gostick J.T., 2017. Versatile and efficient pore network extraction method using marker-based watershed segmentation. Physical Review, 96(2). https://doi.org/10.1103/PhysRevE.96.023307.

Grelk, B., Christiansen, C., Schouenborg, B., Malaga, K., 2007. Durability of Marble Cladding—A Comprehensive Literature. Journal of ASTM Internationl, 4 (4). DOI:10.1520/JAI100857.

Hart, P.E., Nilsson, N. J., Raphael, B., 1968. A formal basis for the heuristic determination of minimum cost paths, in: IEEE transactions on Systems Science and Cybernetics, 4(2), 100-107. DOI: 10.1109/TSSC.1968.300136.

Liang Y., Hu, P., Wang, S., Song, S., Jiang, S., 2019. Medial axis extraction algorithm specializing in porous media. Powder Technology, 343, 512-20. doi.org/10.1016/j.powtec.2018.11.061.

Lindquist, W. B., Lee, S. M., Coker, D. A., Jones, K. W., & Spanne, P., 1996. Medial axis analysis of void structure in three-dimensional tomographic images of porous media. Journal of Geophysical Research: Solid Earth, 101(B4), 8297-8310. https://doi.org/10.1029/95JB03039

Liu J., Pereira G. G., Regenauer-Lieb K., 2014. From characterisation of pore-structures to simulations of pore-scale fluid flow and the upscaling of permeability using microtomography: A case study of heterogeneous carbonates, 2014. Journal of Geochemical Exploration, 144, Part A, 84-96, https://doi.org/10.1016/j.gexplo.2014.01.021.

Ju, M., Li, X., Li, X., Zhang, G., 2022. A review of the effects of weak interfaces on crack propagation in rock: from phenomenon to mechanism. Engineering Fracture Mechanics, 263, 108297. https://doi.org/10.1016/j.engfracmech.2022.108297.

Marini, P., Bellopede, R., 2009. Bowing of marble slabs: Evolution and correlation with mechanical decay. Construction and Building Materials, 23(7), 2599-2605. https://doi.org/10.1016/j.conbuildmat.2009.02.010.

Mauk, M.G., Chiou, R., Genis, V., Carr, E., 2013. Image analysis of microfluidics: Visualization of flow at the microscale. ASEE Annual Conference and Exposition, Conference Proceedings. DOI:10.18260/1-2--19693.

Murru, A., Freire-Lista, D. M., Fort, R., Varas-Muriel, M. J., Meloni, P., 2018. Evaluation of post-thermal shock effects in Carrara marble and Santa Caterina di Pittinuri limestone. Construction and Building Materials, 186, 1200-1211. https://doi.org/10.1016/j.conbuildmat.2018.08.034.

Nicholson, D. T., 2001. Pore properties as indicators of breakdown mechanisms in experimentally weathered limestones. Earth Surface Processes and Landforms: The Journal of the British Geomorphological Research Group, 26(8), 819-838. https://doi.org/10.1002/esp.228.

Nilsson, N. J., 2014. Principles of artificial intelligence. Morgan Kaugfmann.

Ozcelik, Y., & Ozguven, A., 2014. Water absorption and drying features of different natural building stones. Construction and building materials, 63, 257-270. https://doi.org/10.1016/j.conbuildmat.2014.04.030.

Øren, P.E., Bakke, S., 2003. Reconstruction of Berea Sandstone and Pore-Scale Modeling of Wettability Effects, Journal of Petroleum Science and Engineering, 39, 177-199. https://doi.org/10.1016/S0920-4105(03)00062-7.

Pal Arnab Kumar, Siddharth Garia, K. Ravi, Archana M. Nair, 2022. Pore scale image analysis for petrophysical modelling, Micron, 154, 103195. https://doi.org/10.1016/j.micron.2021.103195

Rabbani A., Jamshid S., Salehi S., 2014. An automated simple algorithm for realistic pore network extraction from micro-tomography images. Journal of Petroleum Science and Engineering, 123, 164-171. doi: https://doi.org/10.1016/j.petrol.2014.08.020.

Rabbani A., Babaei M., Shams R., Wang Y. D., Chung T., 2020. DeePore: A deep learning workflow for rapid and comprehensive characterization of porous materials. Advances in Water Resources, 146, 103787. https://doi.org/10.1016/j.advwatres.2020.103787.

Rasolofosaon P.N.J., Siegesmund S., Weiss T., 2000. The relationship between deterioration, fabric, velocity and porosity constraint, in "Proceedings of the 9th International Congress on Deterioration and Conservation of Stone", June 19-24, Venice (Italy), 215-223. https://doi.org/10.1016/B978-044450517-0/50103-3

Russell SJ, Norvig P. 2018. Artificial intelligence a modern approach. Boston: Pearson; ISBN 978-0134610993.

Salina Borello, E., Peter, C., Panini, F., Viberti, D., 2022. Application of A* algorithm for microstructure and transport properties characterization from 3D rock images. Energy, 239, 1222151. https://doi.org/10.1016/j.energy.2021.122151.

Schouenborg, B., Grelk, B., & Malaga, K., 2007. Testing and Assessment of Marble and Limestone (TEAM)--Important Results from a Large European Research Project on Cladding Panels. Journal of ASTM International, 4(5). DOI:10.1520/JAI100855.

Scrivano, S., Gaggero, L., & Aguilar, J. G., 2018. Micro-porosity and minero-petrographic features influences on decay: Experimental data from four dimension stones. Construction and Building Materials, 173, 342-349. https://doi.org/10.1016/j.conbuildmat.2018.04.041.

Shaked D., Bruckstein A. M., 1998. Pruning Medial Axes. Computer Vision and Image Understanding, 69 (2), 156-169. https://doi.org/10.1006/cviu.1997.0598.

Sheppard A.P., Sok R.M., Averdunk H., 2004. Techniques for image enhancement and segmentation of tomographic images of porous materials. Physical A: Statistical Mechanics and its Applications, 339(1), 145–151. https://doi.org/10.1016/j.physa.2004.03.057.

Shorten C., Khoshgoftaar, T. M., 2019. A survey on image data augmentation for deep learning. Journal of Big Data, 6. https://doi.org/10.1186/s40537-019-0197-0.

Sousa, L., Menningen, J., López-Doncel, R., Siegesmund, S., 2021. Petrophysical properties of limestones: influence on behaviour under different environmental conditions and applications. Environmental Earth Sciences, 80(24). DOI:10.1007/s12665-021-10064-3.

Viberti, D., Peter, C., Borello, E. S., Panini, F., 2020. Pore structure characterization through path-finding and Lattice Boltzmann simulation. Advances in Water Resources, 141,103609. https://doi.org/10.1016/j.advwatres.2020.103609.

Wang C., Wu K., Scott G., Akisanya A., Gan Q., Zhou Y., 2020. A new method for pore structure quantification and pore network extraction from SEM images. Energy Fuels, 34, 1, 82-94. https://doi.org/10.1021/acs.energyfuels.9b02522.

Winkler, E. M., 1985. A durability index for stone.

Xiao B., Wang W., Zhang X., Long G., Fan J., Chen H., Deng L., 2019. A novel fractal solution for permeability and Kozeny-Carman constant of fibrous porous media made up of solid particles and porous fibers. Powder Technology, 349, 92-98. https://doi.org/10.1016/j.powtec.2019.03.028.

Xu P., Yu B., 2008. Developing a new form of permeability and Kozeny–Carman constant for homogeneous porous media by means of fractal geometry, Advances in Water Resources, 31(1), 74-81. https://doi.org/10.1016/j.advwatres.2007.06.003.

Xu Z., Lin M., Jiang W., Cao G, Yi Z., 2020. Identifying the comprehensive pore structure characteristics of a rock from 3D images. Journal of Petroleum Science Engineering, 187, 106764. https://doi.org/10.1016/j.petrol.2019.106764. 0920-4105.

List of figure captions

Fig. 1: Thin section in parallel light (left) and in polarized light (right)of the marble C1 (long side is of 1,37 mm).

Fig. 2: Workflow

Fig. 3: Qualitative representation of a thin section image subdivision into subsections. Example of the transversal thin section in which three main groups are identified, each having 3 subsections, along the top row (transv1), middle row (transv2) and bottom row (transv3).

Fig. 4: Qualitative representation of the weathered thin section position with respect to the marble slab and the correspondence between epar sections and transv subsections.

Fig. 5: Images of some subsections from thin sections of impregnated marble, after preliminary image processing: (a) non- weathered, (b) epar2, (c) epar3, (d) transv (middle), (e) transv (bottom - center).

Fig. 6: Binarization process: (a) image from thin section, after preliminary image processing; (b) superposition of image and binary mask; (c) downsampled binary image.

Fig. 7: Schematic representation of the approach used to increase algorithm exploration in poorly connected areas: (a) original binarized image; (b) image subdivision into 36 sub-windows; (c) example of path creation result within an individual sub-window; (d) final output image that accounts for the contribution of all the 36 sub-windows; (e) path creation along the main four directions (N-S, S-N, E-W, W-E) and path merging within a sub-window (right).

Fig. 8: Qualitative representation of pore throat description along a path. At each path node individuated by A* the pore size is calculated perpendicularly to the local path direction. Only a few path nodes are shown as example.

Fig. 9: Examples of paths identified within the porous structure of the binarized images: (a) non- weathered, (b) epar2, (c) epar3, (d) transv (middle), (e) transv (bottom - center).

Fig. 10: Comparison of pore radius distribution (a) in the horizontal sections before and post weathering, and (b) in the three subdivisions (top, middle, bottom) of the transversal sections of the weathered sample.

Fig. 11: Statistical comparison between the horizontal and vertical subsections: (a) Pore radius distribution; (b) porosity distribution. The vertical lines represent the mean values, the box limits are the P25 (left) and the P75 (right) values while the line limits represent the P10 (left) and the P90 (right).

Table. 1: Final results of UPV measurements: Velocities (v), standard deviation (St. dev.) and variations between non-weathered and weathered specimen (Δv) at different ultrasound oscillation frequencies (f).

Specimen	f = 33 kHz			f=250 kHz		
	v [m/s]	St. dev. [m/s]	Δv [%]	v [m/s]	St. dev. [m/s]	Δv [%]
non-weathered	2422	54	-16,43	3823	12	-42,32
weathered	2024	187		2205	193	

Table. 2: Flexural strength (σ) test results.

Specimen	σ [MPa]	St.dev. [MPa]	Δ σ [%]
non-weathered	12,9	4,5	-28,48
weathered	9,2	1,9	

Table. 3: Final values of the water absorption capacity (WA) obtained by means of contact sponge.

Specimen	W A $\left[\frac{g}{cm^2 \cdot min}\right]$	St. dev. $\left[\frac{g}{cm^2 \cdot min}\right]$	Δ W A [%]
non-weathered	3,37E-03	1,69E-03	293,75
weathered	1,33E-02	8,05E-03	

513 Table. 4: Final values of the water absorption capacity (Ab) obtained at atmospheric pressure.

Specimen	Ab [%]	St.dev. [%]	Δ Ab [%]
non-weathered	0,186	0,072	203,49
weathered	0,564	0,065	

514

515

516

517 Table. 5: Percentile values of the porosity distribution.

Section	Porosity (%)				
	P10	**P25**	**P50**	**P75**	**P90**
Initial	5.3467	8.1283	14.5186	21.8309	23.5754
Epar1	17.8861	18.1874	22.3606	26.8697	28.3669
Epar2	16.8431	17.9868	19.5253	23.8747	31.5994
Epar3	20.7917	22.0146	27.5460	28.5460	28.5814
Transv1	6.3058	7.8469	12.4700	20.2944	22.9025
Transv2	10.6411	10.7863	11.2219	18.0451	20.3194
Transv3	18.7181	20.0354	23.9875	26.2819	27.0467

518

519 Table. 6: Percentile values of the pore radius distribution.

Section	Pore Radius Distribution (μm)				
	P10	**P25**	**P50**	**P75**	**P90**
Initial	4	5.6569	10	16.9706	26
Epar1	4	6	11.3137	16.9706	28.2843
Epar2	4	6	10	16.9706	28
Epar3	4	8	12	20	33.9411
Trasnv1	2.8284	5.6569	8.4853	16	26
Transv2	2.8284	5.6569	8.4853	14.1421	24
Transv3	4	6	10	16.9706	30

520
521

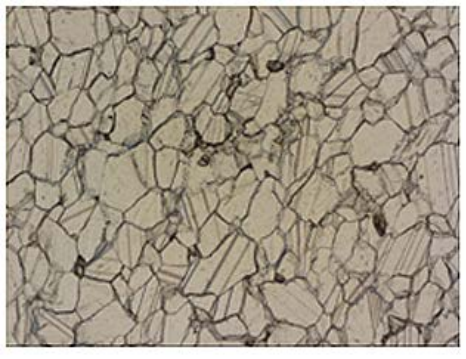

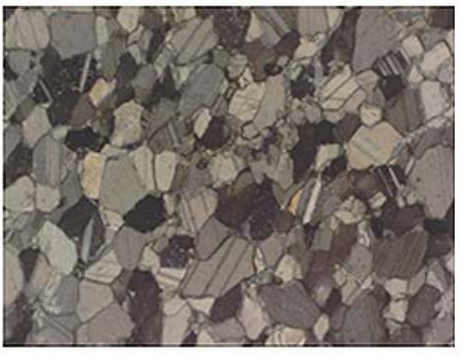

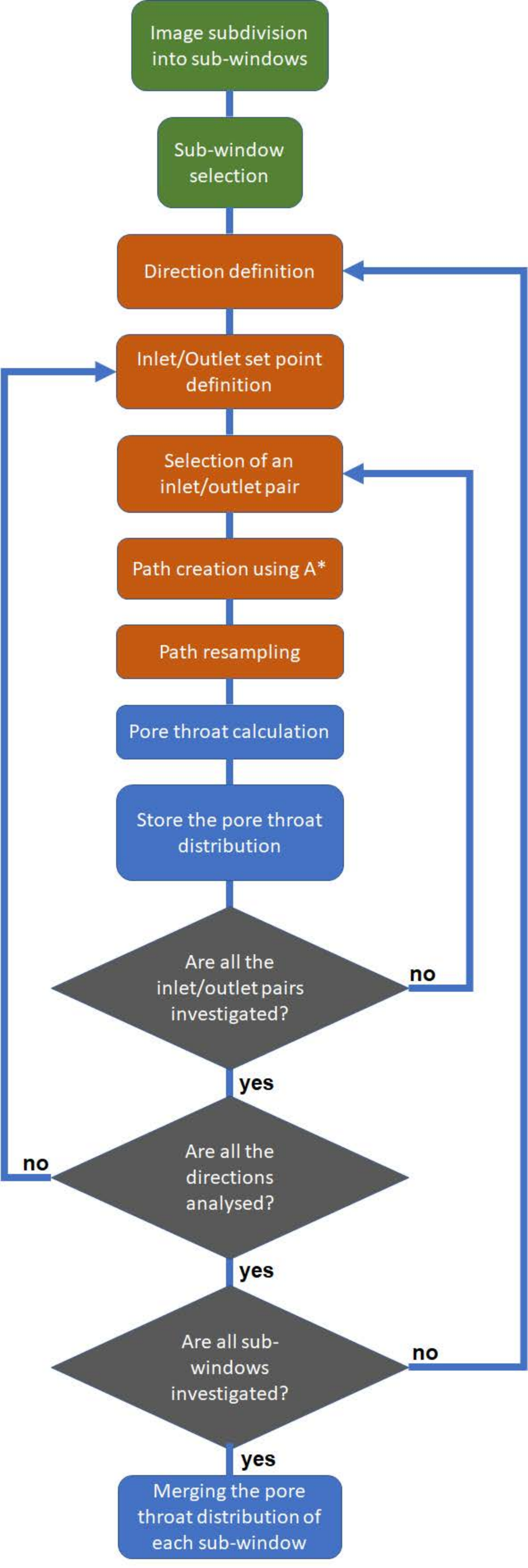
Image subdivision into sub-windows
Sub-window selection
Direction definition
Inlet/Outlet set point definition
Selection of an inlet/outlet pair
Path creation using A*
Path resampling
Pore throat calculation
Store the pore throat distribution
Are all the inlet/outlet pairs investigated?
no
yes
Are all the directions analysed?
no
yes
Are all sub-windows investigated?
no
yes
Merging the pore throat distribution of each sub-window

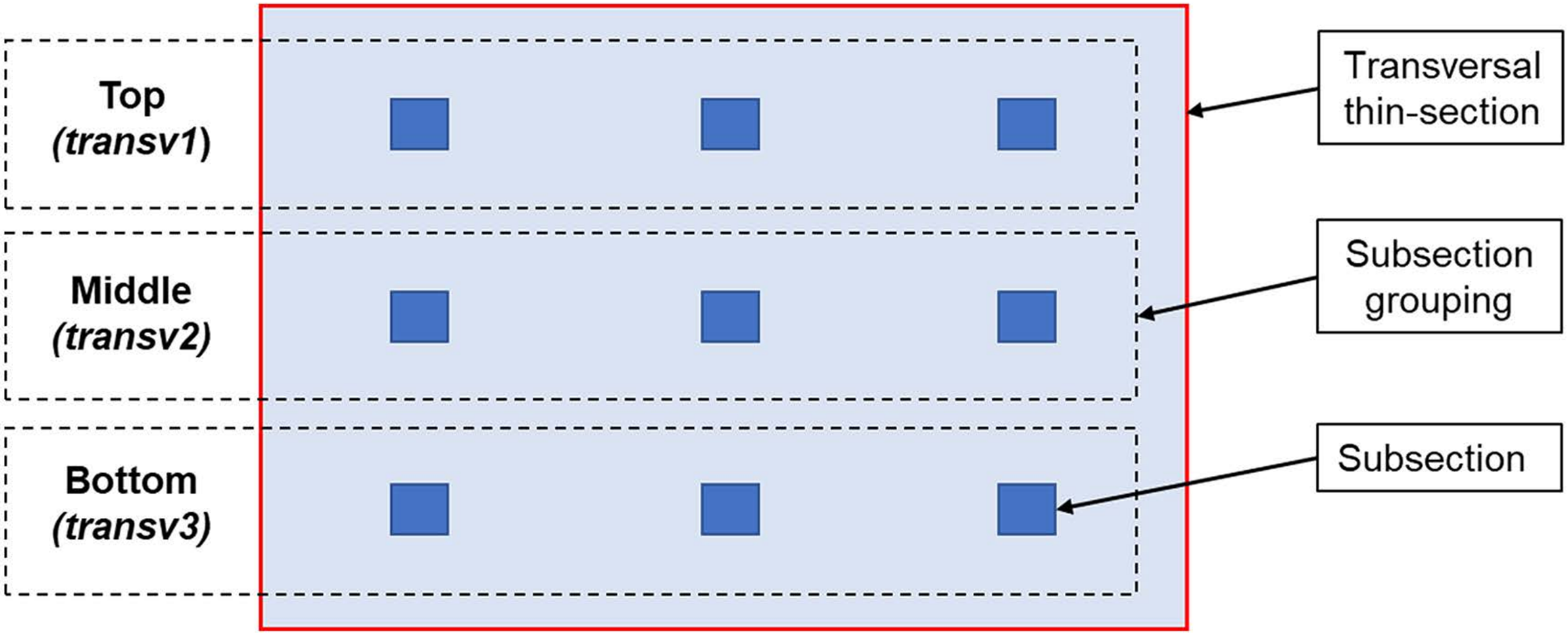
Top
(transv1)
Middle
(transv2)
Bottom
(transv3)
Transversal thin-section
Subsection grouping
Subsection

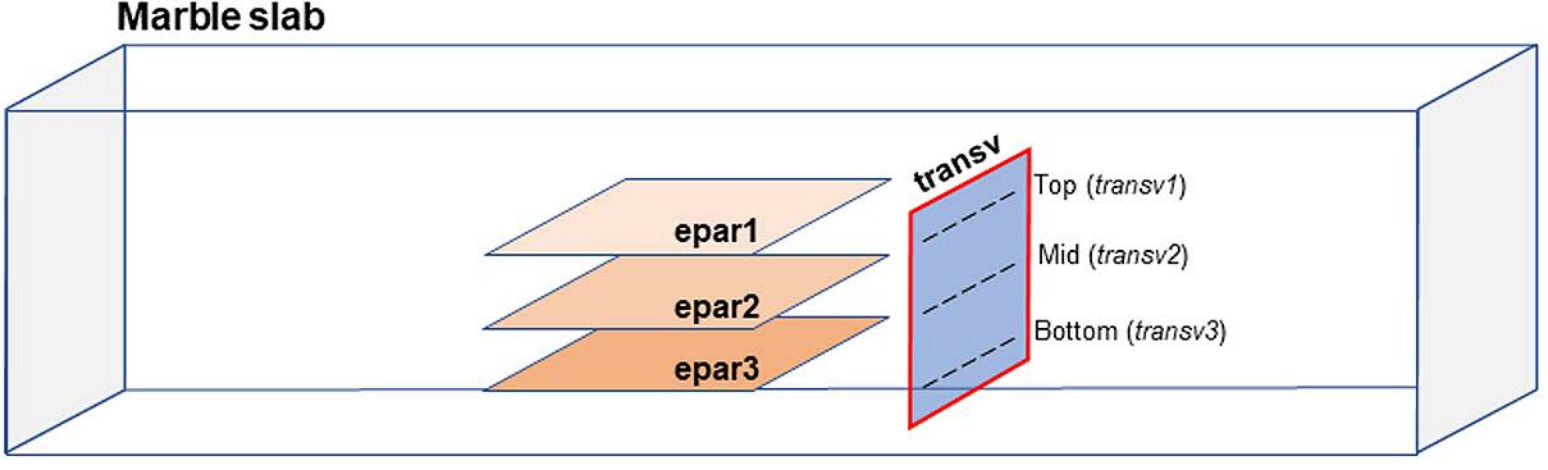
Marble slab
epar1
epar2
epar3
transv
Top (transv1)
Mid (transv2)
Bottom (transv3)

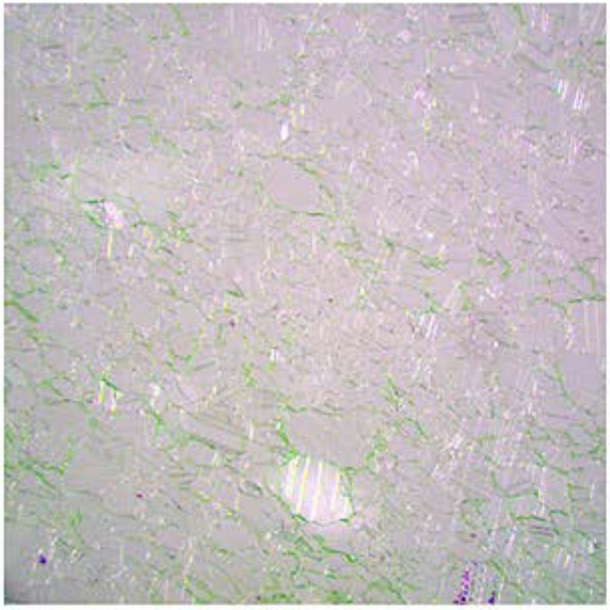

(a)

0.5 mm

Grain

Impregnated pore

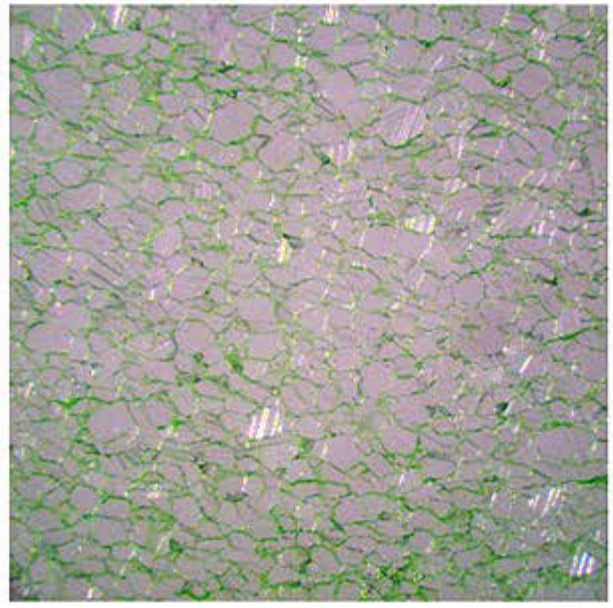

(b)

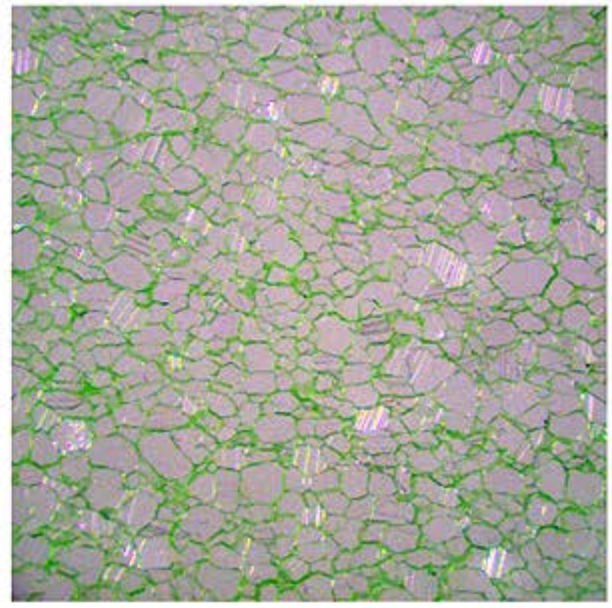

(c)

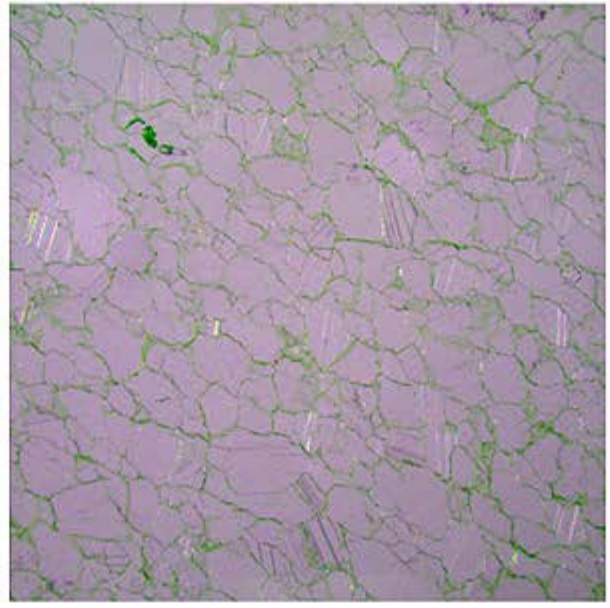

(d)

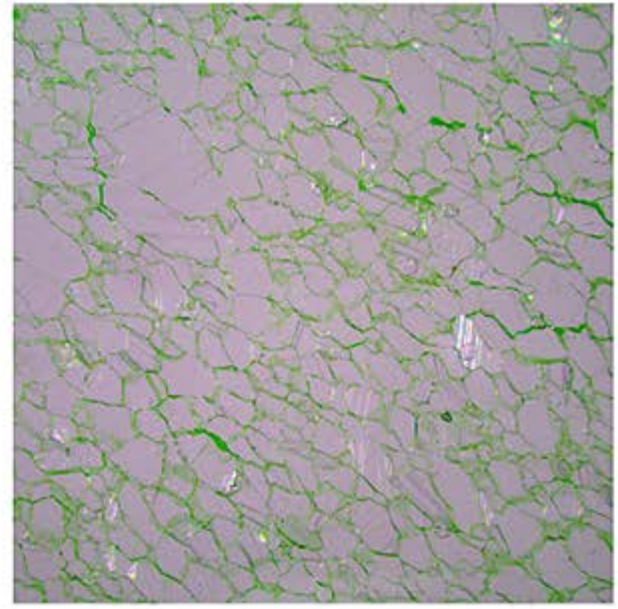

(e)

(a)

(b)

(c)

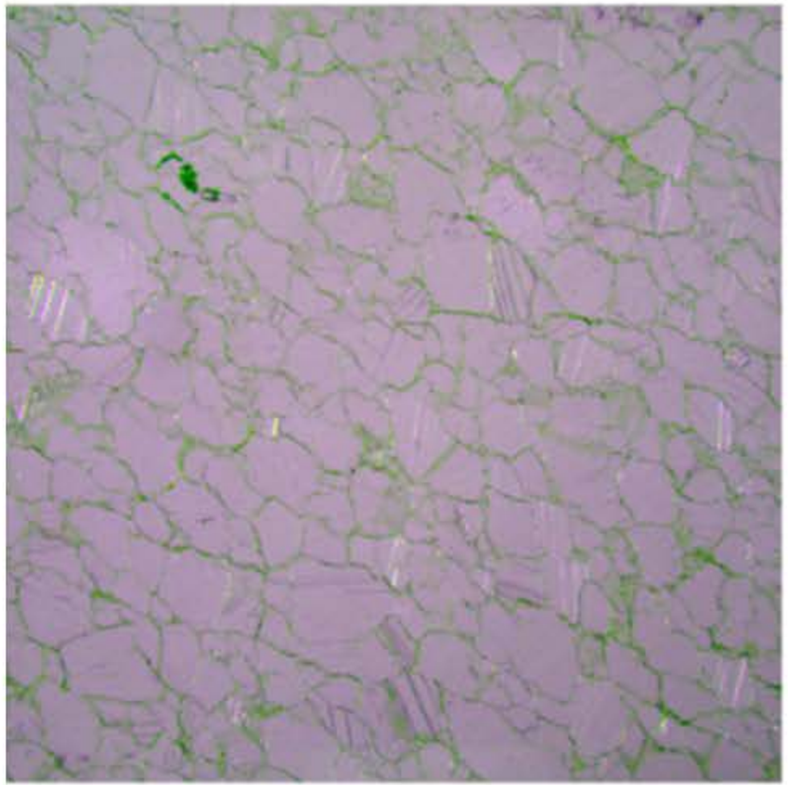

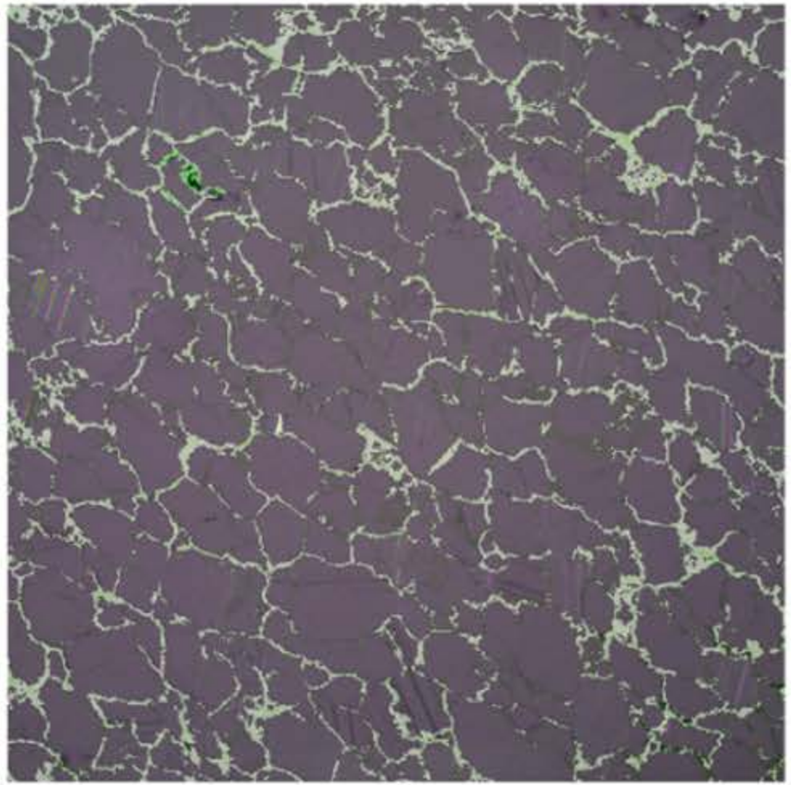

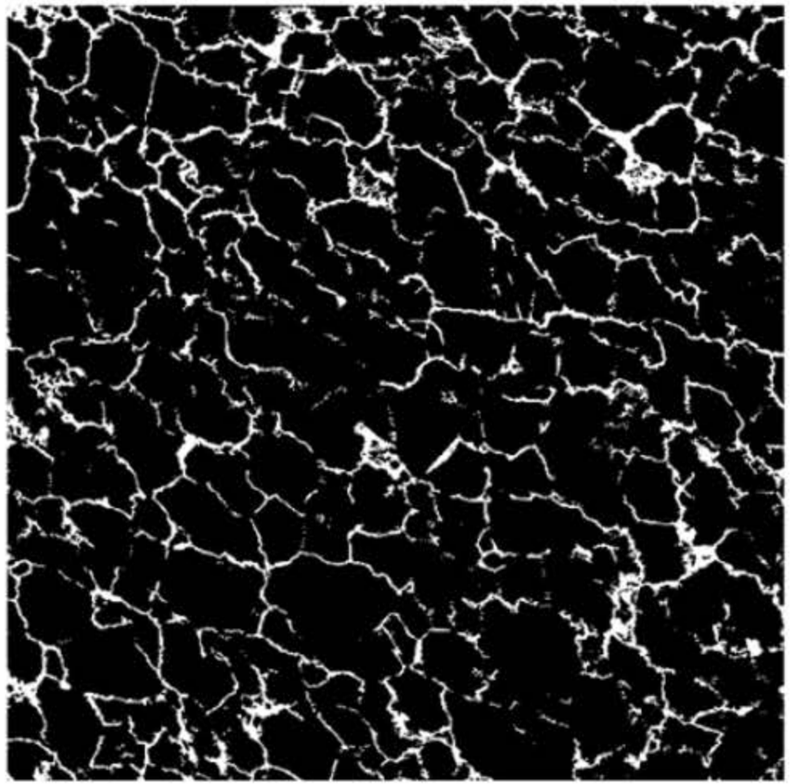

Grains

Impregnated path

0.5 mm

Mask

Grains

Pores

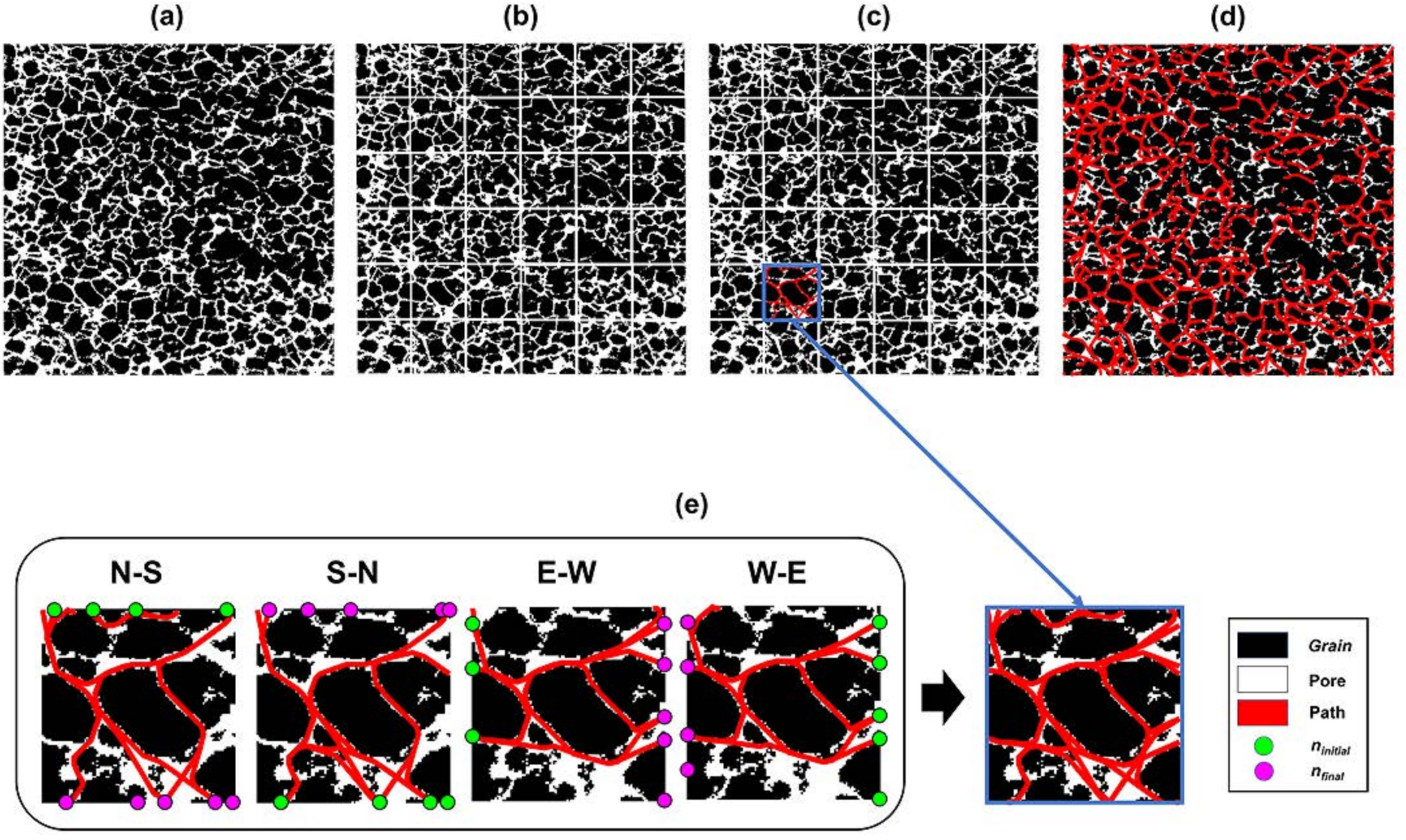
(a)
(b)
(c)
(d)
(e)
N-S
S-N
E-W
W-E
Grain
Pore
Path
$n_{initial}$
n_{final}

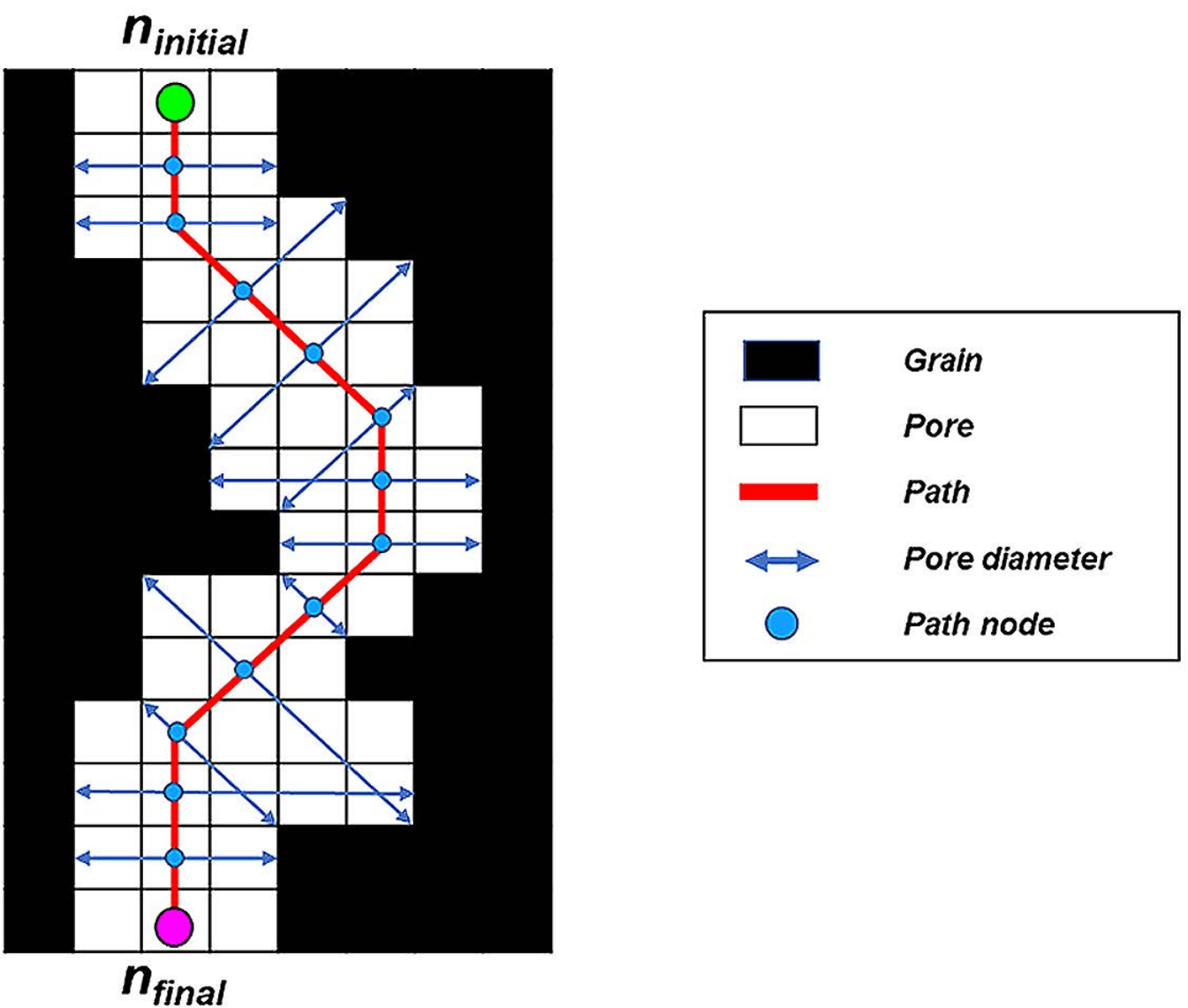
$n_{initial}$
n_{final}
Grain
Pore
Path
Pore diameter
Path node

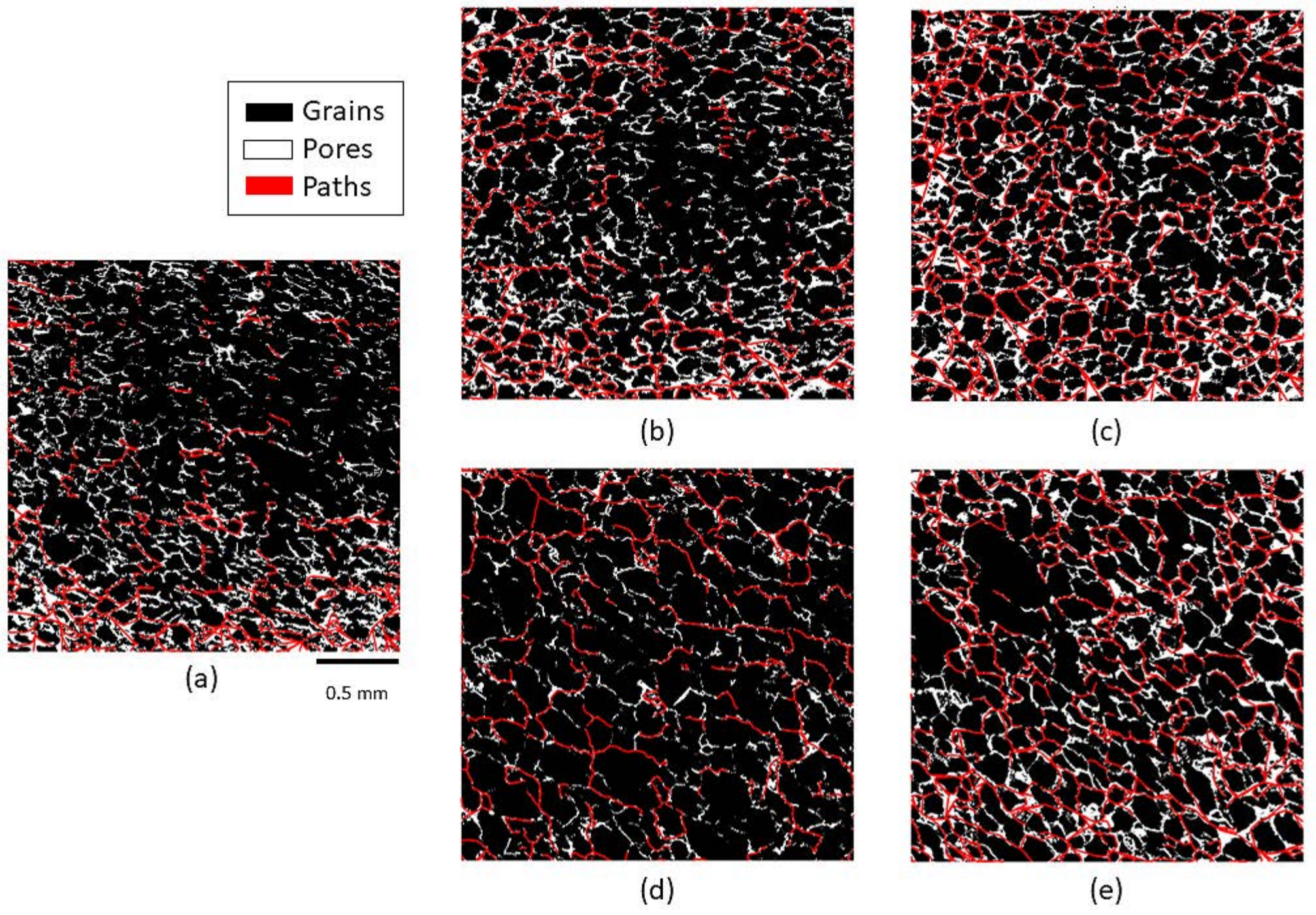
Grains
Pores
Paths
(a)
0.5 mm
(b)
(c)
(d)
(e)

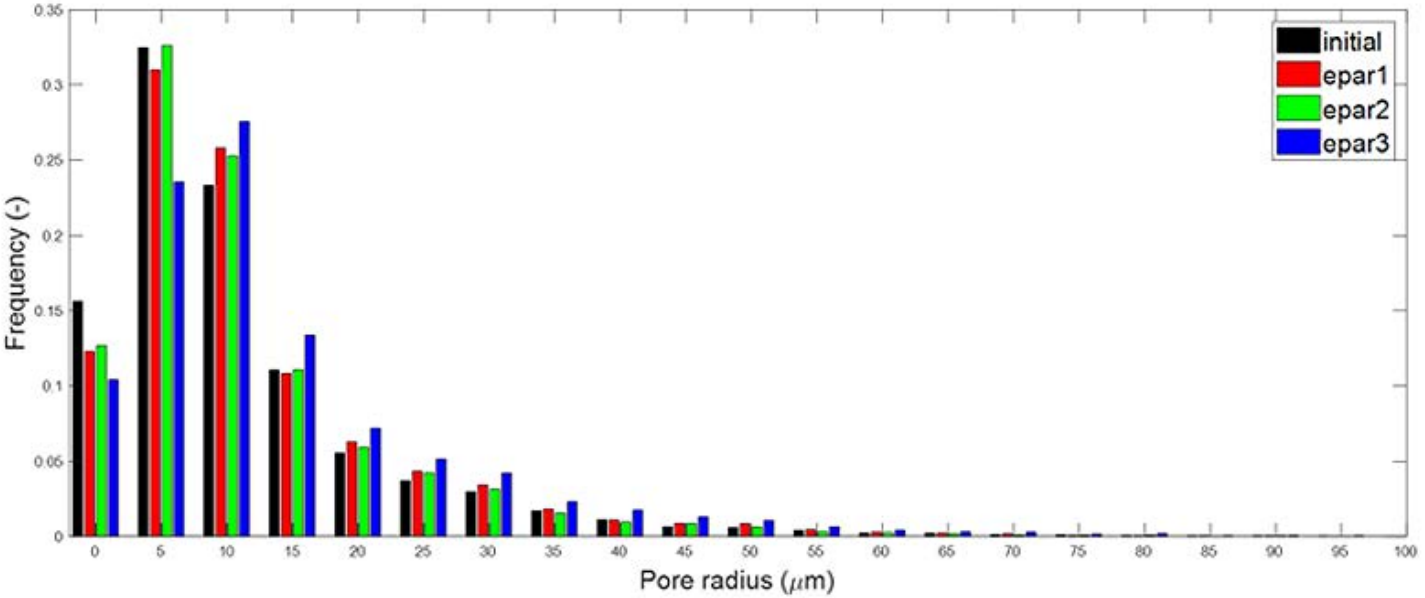
initial
epar1
epar2
epar3
Frequency (-)
Pore radius (μm)

(a)

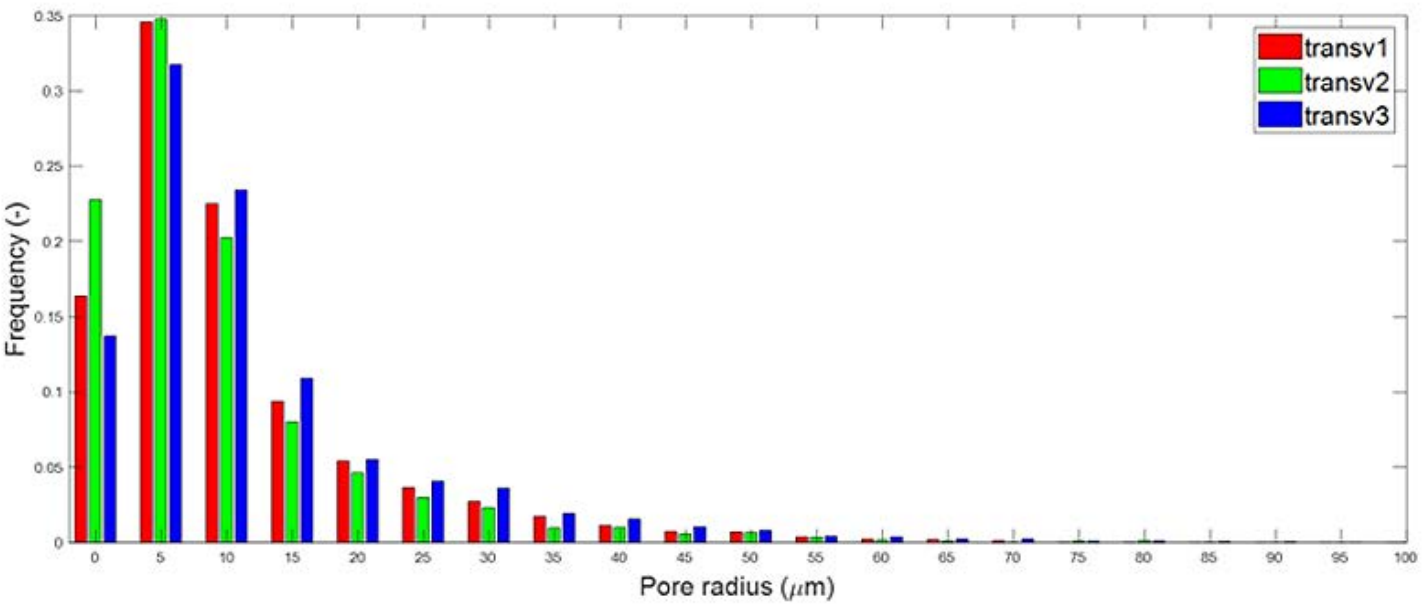
transv1
transv2
transv3
Frequency (-)
Pore radius (μm)

(b)

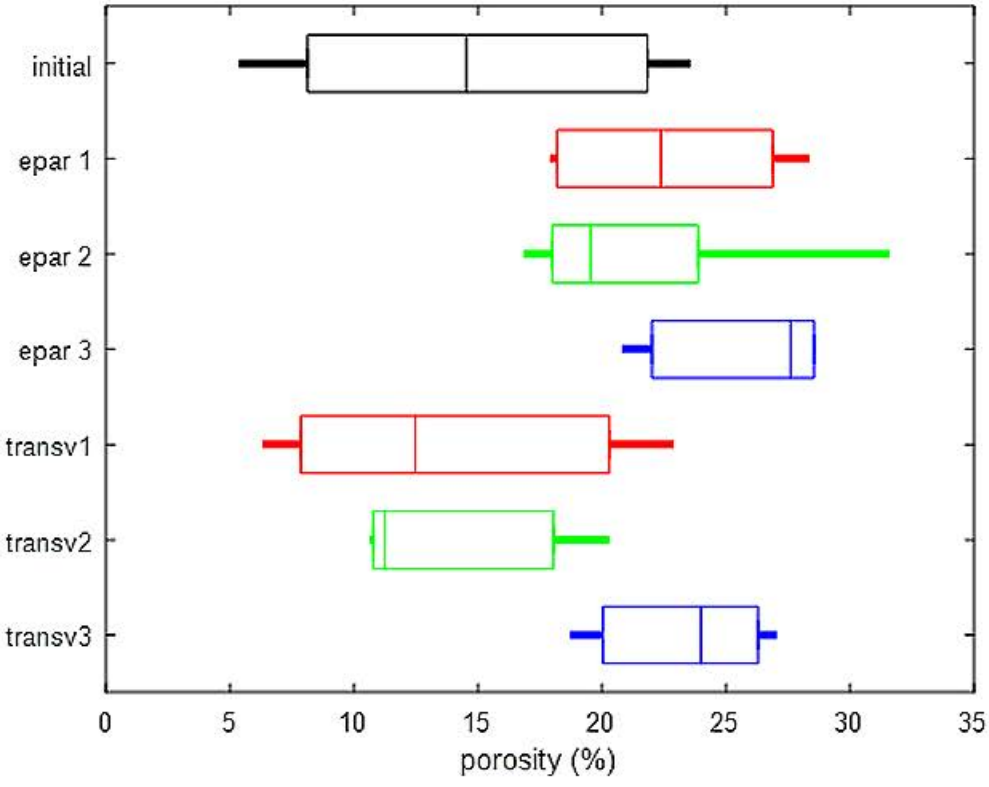
initial
epar 1
epar 2
epar 3
transv1
transv2
transv3
0
5
10
15
20
25
30
35
porosity (%)

(a)

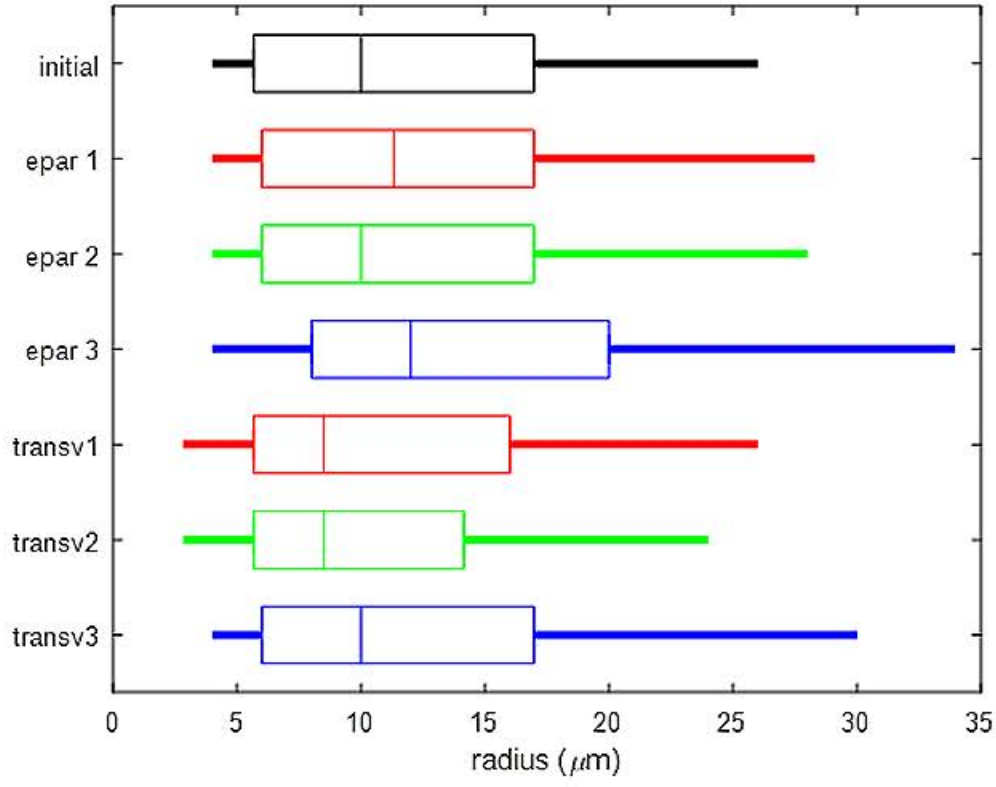
initial
epar 1
epar 2
epar 3
transv1
transv2
transv3
0
5
10
15
20
25
30
35
radius (μm)

(b)